Bulletin of the Seismological Society of America, Vol. 95, No. 1, pp. 173–184, February 2005, doi: 10.1785/0120030251

Ⓔ

Using the Effects of Depth Phases on *P*-wave Spectra to Determine Earthquake Depths

by Linda M. Warren and Peter M. Shearer

Abstract For shallow earthquakes, the surface-reflected depth phases (*pP* and *sP*) arrive shortly after the primary arrival, and the time separation among the three phases can be used to determine the origin depth of the earthquake. To model the relative arrival times and amplitudes of these phases, and the core reflections and water-column reverberations for a given earthquake, we construct stick seismograms using the IASPEI91 velocity model and the Harvard CMT focal mechanisms at the distances and azimuths of the recording seismometers. While the differing arrival times and amplitudes are features observable in the time series, they also affect the spectrum, and we compute the spectrum for a time window that includes the *P* wave and subsequent arrivals. We quantify the effects of variations in these properties over the focal sphere in terms of differences in the slope of the log spectrum at different stations. To determine the depth of an earthquake, we compare our observed spectral variations with the predicted spectral variations for earthquakes originating at depths within 30 km of the PDE depth and identify the depth with the smallest L1 misfit as the true earthquake depth. We demonstrate the effectiveness of this method by applying it to a group of 35 thrust earthquakes in the Aleutian arc near the Andreanof Islands, but we also describe some complications introduced by strongly directive ruptures, as illustrated for the 1995 Jalisco, Mexico, event.

Online material: Observed and predicted variations in pulse width for Aleutian Island earthquakes.

Introduction

Accurate determination of earthquake depth is necessary for assessing seismic hazard, descriminating earthquakes from nuclear explosions, interpreting Earth structure, and understanding tectonic processes. The depth of an earthquake can be difficult to obtain because it trades off with event origin time and can be biased by lateral heterogeneities in Earth structure.

Many methods of locating earthquakes have been developed to reduce these errors and are routinely used in earthquake studies. For example, the relative locations of similar earthquakes, which can be resolved by cross-correlating waveforms to find differential travel times to stations between events, are useful for delineating fault structures.

The identification of an absolute depth requires the actual travel times of various phases to a number of stations rather than the differential times between events, as well as knowledge of the velocity structure around the earthquake. Using an appropriate focal mechanism and velocity model, the earthquake depth can be found through waveform modeling (Sipkin, 2000). In particular, the travel-time delay between the primary arrival and the depth phases constrains the depth (Engdahl *et al.*, 1998). Cepstral methods (Cohen, 1970; Childers *et al.*, 1977; Bonner *et al.*, 2002), which estimate the frequencies of the spectral holes created by these reverberations, can also be used to resolve earthquake depth.

In this article, we present a method that employs a frequency-domain stacking technique to determine the absolute depth of earthquakes based on the time delay between the primary and depth-phase arrivals and their amplitudes at many seismic stations world-wide. Using the IASPEI91 velocity model (Kennett, 1991) and Harvard CMT solutions, we generate synthetic seismograms showing the relative times and amplitudes of these phases for earthquakes at different depths. Next, we compute the effects the varying times and amplitudes have on the spectrum at different stations, and correlate these predictions with observed variations in spectral content to determine the earthquake depth. This method, which is automated to calculate variations in frequency content between stations for each earthquake, is faster than measuring the arrival times and amplitudes of each phase at many stations. In addition, our stacking technique accounts for the source-time function and attenuation

anomalies without first explicitly describing them or their form. In the following sections, we describe the method and apply it to some recent earthquakes.

Data and Processing

A database of long-period seismograms (sampled 1/sec) from globally-distributed, $m_b \geq 5.5$ earthquakes is maintained online at Scripps (see Bolton and Masters, 2001, for a detailed database description). Beginning with records from 1988, we select *P*-wave arrivals observed between 20° and 98° with signal-to-noise ratios (SNRs) ≥3. The SNR, which we define as the ratio of the largest amplitude in the 64-sec-long time window from which we compute the spectrum to the largest amplitude during the preceding 64 sec, is chosen to allow sufficient focal sphere coverage while maintaining a strong signal in the seismograms. After we identify the seismograms that fit these criteria, we compute the spectrum around each *P*-wave arrival with a multitaper method (Thomson, 1982; Park *et al.*, 1987). We use a time-bandwidth product of 1.5 and two orthogonal tapers, so the resulting spectra have a small amount of smoothing. Each spectrum is computed for a 64-sec-long window that begins 15 sec before the arrival time predicted by IASPEI91 (Kennett, 1991), although varying the position of this window by up to several seconds does not significantly change the results. While this timing emphasizes the *P*-wave arrival, the computed spectrum is also influenced by other factors, such as the arrivals of additional phases and source- and path-specific effects. We will solve and then correct for the source- and path-specific effects, leaving spectral changes caused by the relative timing and amplitudes of the later arrivals. These remaining spectral variations let us determine earthquake depths.

Spectral Components

Depth Phases and Core Reflections

Our signal window includes 49 sec of the seismogram after the predicted *P*-wave arrival time. Depending on the earthquake depth and the epicentral distance to the station, depth phases and core reflections may also arrive within this time window. While in theory one could measure the separation between these phases in the time domain to find the depth of an earthquake, there is not always a clear signal at short periods and, at longer periods, the depth phases are not directly separable from the direct phases. However, the later arrivals will change the apparent frequency content of the *P* wave in a predictable manner based on earthquake depth and focal mechanism, and we use these spectral variations to constrain earthquake depth.

To investigate the effect of the arrivals of other phases within the signal window, we generate stick seismograms using geometrical ray theory and the appropriate surface and core-mantle-boundary reflection coefficients from IASPEI91 (Kennett, 1991) for the predicted arrival times and amplitudes of *P, pP, sP, PcP, pPcP,* and *sPcP* for stations at various azimuths and distances for a given focal mechanism and earthquake depth. Tests we performed of this method versus full reflectivity synthetics are generally in good agreement. For earthquakes beneath the oceans, we also include the *pwP* and *swP* arrivals in our synthetics. Synthetic seismograms for uniformly-distributed azimuths and ranges are shown in Figure 1 for a 20-km-deep thrust earthquake with a focal mechanism representative of those in the Aleutian region that we will discuss later. For this example, we have not included a water layer. The depth phases (*pP* and *sP*) often have the largest amplitudes, while the core-reflected phases and water-column reverberations, when included, are usually small. On a given seismogram, the core-reflected phases are usually 1%–8% of the largest of the *P, pP,* and *sP* amplitudes, although they are occasionally as large as 25%. Small *P*-wave amplitudes can be seen along the nodal planes (such as at an azimuth of 216° and range of 50°). Other source mechanisms show similar patterns, both in terms of the magnitude of the spectral variations, the focal-sphere distance over which they occur, and the rapid changes with earthquake depth.

We compute the spectra of the synthetic seismograms beginning 15 sec before the *P*-wave arrival. Since we input a delta function for the source-time function, the spectrum for just the *P* wave should be flat. Looking across a wide-frequency band, the spectra, which are plotted in Figure 2, have holes at frequencies determined by the earthquake depth and radiation pattern. Cepstral methods use the frequencies of these holes to identify earthquake depth. We focus on a narrower frequency band, between 0.039 and 0.086 Hz (12–26 sec), to observe the effect that earthquake depth has on the log spectra. As shown in Figure 2b, some of the spectra (which are plotted with the stacked trend removed to highlight the variations in frequency content) are enriched in high-frequency energy relative to others. This difference in frequency content, which we measure with the slope of the log spectra, is spatially coherent over the focal sphere (Fig. 3). However, as the earthquake depth is varied, there are changes in the focal sphere locations that are enriched and depleted in high-frequency energy. There are noticeable differences in the focal-sphere patterns for earthquakes separated by as little as 5 km in depth.

Adding a water layer dramatically changes the patterns of predicted variation in frequency content for earthquakes less than ~10 km deep. For deeper events, the focal-sphere locations enriched or depleted in high-frequency energy are similar whether or not there is an overlying water layer, and the magnitudes of the variations change only slightly. The differences decrease with increasing earthquake depth. The thickness of the water layer has a smaller effect on the focal sphere variations than the presence or absence of a water layer.

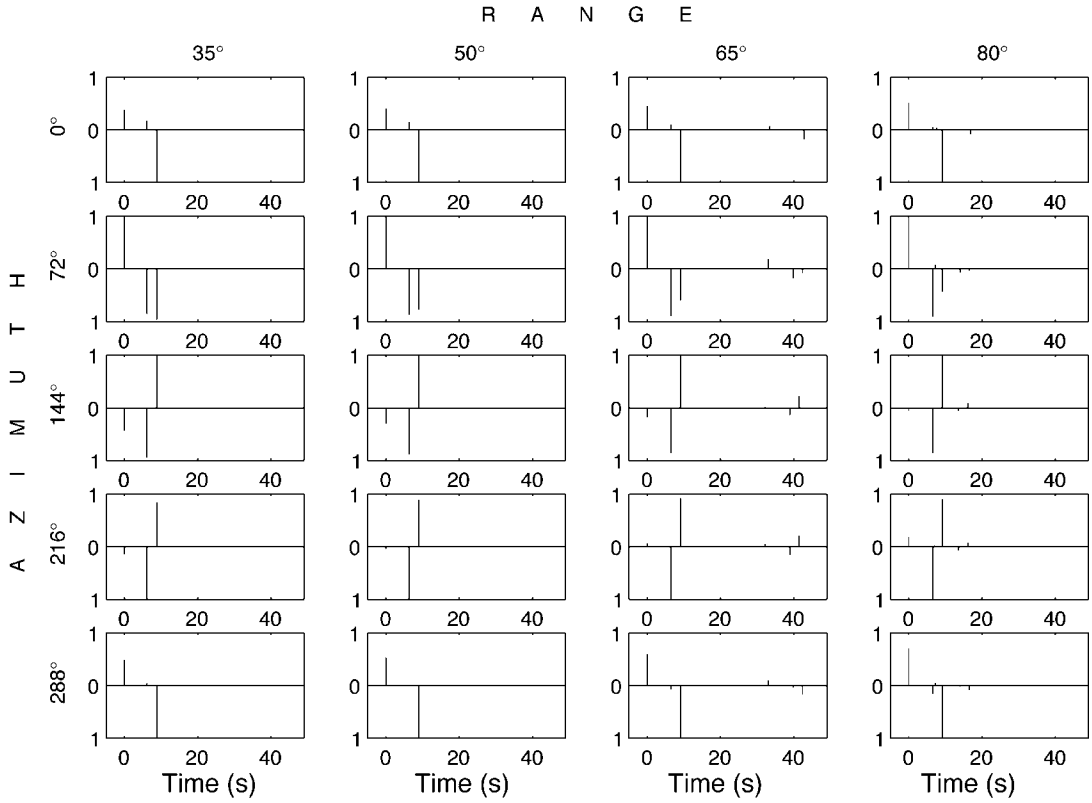

Figure 1. Stick seismograms showing variations in amplitudes of depth phases and core reflections at uniformly-distributed azimuths and ranges, as indicated in the figure, for a 20-km-deep earthquake with focal mechanism similar to that of the Andreanof Islands earthquakes (strike 261°, dip 27°, rake 112°). This example does not include a water layer.

For earthquakes deeper than ~150–200 km, Figure 3 shows that the variations in spectral content caused by other phases are negligibly small. This is mainly because the depth phases do not arrive within the studied time window. While *PcP* arrives in this time window for some epicentral distances, its effect is small because its amplitude is generally less then 8% of the amplitude of the *P* wave. Thus, for a 64-sec-long time window, we cannot use spectral variations from depth-phase interference to determine earthquake depths for deep events.

For earthquakes shallower than ~150–200 km, the coherent patterns in variations in spectral content and the relatively fast changes with depth suggest that we can improve earthquake depths by comparing our observed variations in frequency content with predicted variations for earthquakes at different depths. We will compare the observations with predictions for earthquakes located at the catalog depth, ±30 km, in 2 km increments. For the above example of a 20-km-deep earthquake, we use the synthetic spectral variations as our observations, and correlate the spectral-slope measurements with the predicted variations for earthquakes at depths ranging from the surface to 50 km. At each depth tested, the correlation coefficient and the L1 and L2 misfits are plotted in Figure 4. We define the L1 misfit as

$$m_{L1} = \frac{\sum_{i=1,n} |s_{pred}(i) - s_{obs}(i)|}{n - 1} \quad (1)$$

and the L2 misfit as

$$m_{L2} = \sqrt{\frac{\sum_{i=1,n} |s_{pred}(i) - s_{obs}(i)|^2}{n - 1}}, \quad (2)$$

where $s_{obs}(i)$ is the log of the observed spectral slope at station i, $s_{pred}(i)$ is the log of the predicted spectral slope at station i, and n is the total number of stations. There is a peak in the correlation coefficient, as well as minima in the misfits, for an earthquake located at 20 km depth. Earthquakes at other depths do not explain the observations nearly as well.

Reasonable errors in the assumed earthquake focal mechanism do not change the estimated depth of the earthquake. For this example, if the strike of the fault is rotated by 20°, the depth corresponding to the maximum correlation coefficient and minimum misfit is still 20 km. Generally, focal mechanism errors cause the correlation coefficients to decrease and misfit values to increase slightly at each depth,

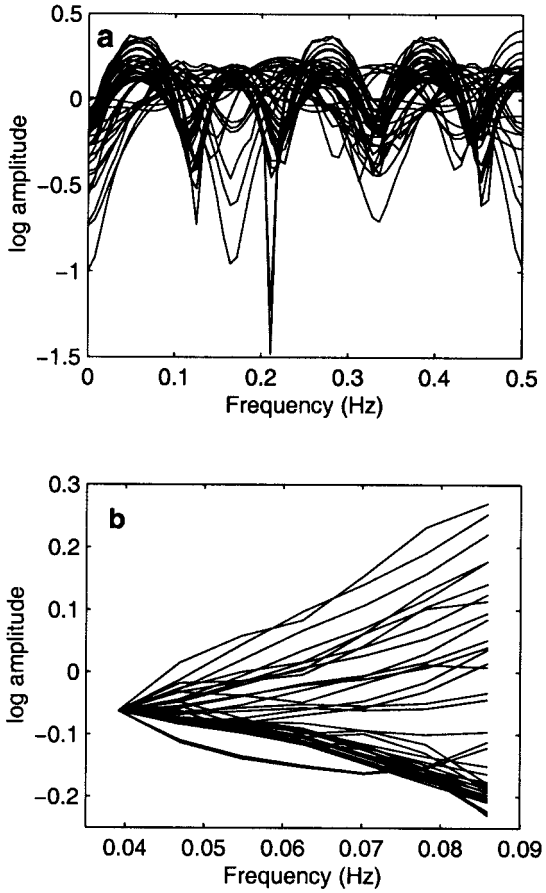

Figure 2. Log spectra of stick seismograms in Figure 1 and, for increased focal-sphere coverage, 20 additional uniformly-distributed stick seismograms for the same focal mechanism. (a) Over a wide frequency band, the holes in the spectra are controlled by earthquake depth and radiation pattern. (b) Focusing on a narrower frequency band (0.039–0.086 Hz) and removing the stacked trend, the effects of earthquake depth and focal mechanism are seen as differences in the log spectral slope between stations located at different azimuths and ranges. The differences in the log spectral slope can be used to determine earthquake depth.

as shown in Figure 4. At 20 km depth, the correlation coefficient decreases to 0.909 (from 1.0) and the minimum misfits increase a little from zero.

To estimate errors in the earthquake depths, we use bootstrap resampling (Efron, 1982) of the observed variations in spectral slope. We calculate the mean and standard error from the depth with the lowest L1 and L2 misfits and largest cross-correlation coefficients for 100 combinations of the observations. Usually the best depths cluster around one depth. However, sometimes the depths cluster in two (or more) distinct groups, and we calculate the mean and standard error for each group separately and report these values for depths found $\geq$5% of the time. We generally select the depth with the lowest L1 misfit and highest bootstrap-resampling percentage as the true earthquake depth.

Rupture Directivity and Other Source Complexity

While the method we describe is relatively insensitive to errors in the focal mechanism, it can be strongly affected by source complexity. For example, over the narrow frequency band that we study, the spectral variations caused by the interference from the depth phases can appear similar to the spectral shifts that would be caused by a directive rupture. If an earthquake rupture propagates predominantly in one direction, the radiated waves are Doppler-shifted (Haskell, 1964; Bollinger, 1968), resulting in predictable variations in frequency content over the focal sphere. In the direction of rupture propagation, the spectra are enriched in high frequencies, while in the opposite direction they are depleted in high-frequency energy. As a result, a directive rupture also results in coherent patterns of more and less high-frequency energy over the focal sphere. For example, if the synthetic earthquake discussed above ruptures updip along the shallowly-dipping plane of the focal mechanism, the spectral variations due solely to the directivity of the rupture are plotted in Figure 5. The magnitude of the variations increases with increasing earthquake magnitude and fault length. As a result, the spectral variations from smaller earthquakes, which rupture shorter faults, will tend to be negligibly small. Unlike for depth-phase interference, the focal sphere regions enriched or depleted in high-frequency energy do not change with earthquake depth.

Studying 25 large ($M_w \geq 7$), shallow ($\leq$50 km) earthquakes, McGuire *et al.* (2002) found that 80% of these events demonstrated a primarily unilateral rupture. While smaller earthquakes, which make up a large portion of our catalog, may be less likely to rupture unilaterally and will have a smaller directivity signal if they do rupture unilaterally, this potential spectral contaminant must be considered, since depth-phase interference and rupture directivity can result in similar amounts of spectral variation. However, the focal-sphere locations enriched or depleted in high-frequency energy generally will differ for the two effects, and we can test whether the observed spectral variations are consistent with depth-phase interference alone. When the observations and predictions are compared, as for the synthetic example above, a directive rupture will often lower correlation coefficients and raise misfits in the earthquake-depth determination.

In Figure 3 and subsequent figures showing spectral variations over the focal sphere, we have followed Warren (2003) to translate the measurements of the relative slopes of the log spectra to the variations in pulse width they would correspond to if the spectral changes resulted entirely from directivity. While the spectral variations reflect a combination of directivity and depth-phase effects, the pulse width on a given seismogram can be quantified independent of other records, while the depth determination relies on multiple records.

Earthquakes composed of multiple subevents can affect the spectrum in a similar way, again interfering with our

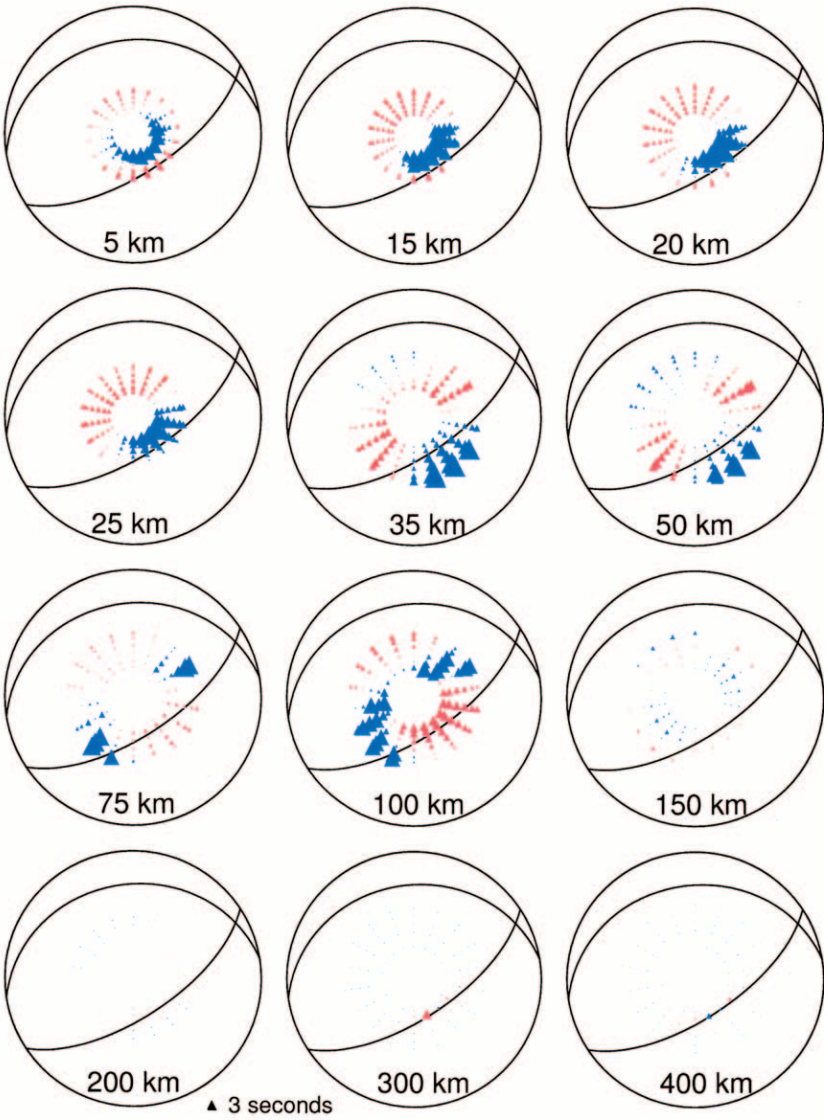

Figure 3. For a given focal mechanism, the interpretation of depth-phase and core-reflected arrivals in terms of rupture directivity changes with earthquake depth. For the focal mechanism used to construct the synthetics in Figures 1 and 2, the patterns for earthquakes at depths ranging from 5 km to 400 km, as labeled in the figure, are plotted. Red indicates longer than average pulse widths (i.e., depleted in high frequencies) while blue indicates shorter than average pulse widths (i.e., enriched in high frequencies). The size of the symbol is proportional to the pulse-width anomaly.

ability to determine the earthquake depth. For these events, the effect may be even more complicated if the focal mechanism changes during rupture.

Source-Time Function and Attenuation

The stick seismograms we generate, with a delta function representing the source-time function of each earthquake and no attenuation as the waves propagate through the Earth, are simplifications. However, we can account for variable source-time functions and attenuation in the data with the stacking procedure of Warren and Shearer (2000). Each computed spectrum $U(f)$ is the convolution of source $S(f)$, receiver $R(f)$, instrument $I(f)$, and propagation $A(f)$ response functions:

$$U(f) = A(f)\, S(f)\, R(f)\, I(f) \,/\, G, \qquad (3)$$

with the amplitude scaled by the geometrical spreading factor G. We take the log of the spectrum and correct for a theoretical source model $\bar{S}$ with an ω^{-2} falloff at high frequencies (Houston and Kanamori, 1986), the PREM attenuation model $\bar{A}$ (Dziewonski and Anderson, 1981), and the known instrument response:

$$\log \tilde{U} = \log U - \log \bar{S} - \log \bar{A} - \log I, \qquad (4)$$

leaving deviations from the theoretical source and attenuation models. Since we have multiple receivers for each earthquake and multiple earthquakes for each station, we can approximate the source- (T) and receiver-side (R) variations by stacking the appropriate spectra. For the ith earthquake and the jth station, we have

$$\begin{aligned} \log T_i &= \frac{1}{N} \sum_{j=1,N} [\log \tilde{U}_{ij} - \log R_j] \\ \log R_j &= \frac{1}{M} \sum_{j=1,M} [\log \tilde{U}_{ij} - \log T_i] \end{aligned} \qquad (5)$$

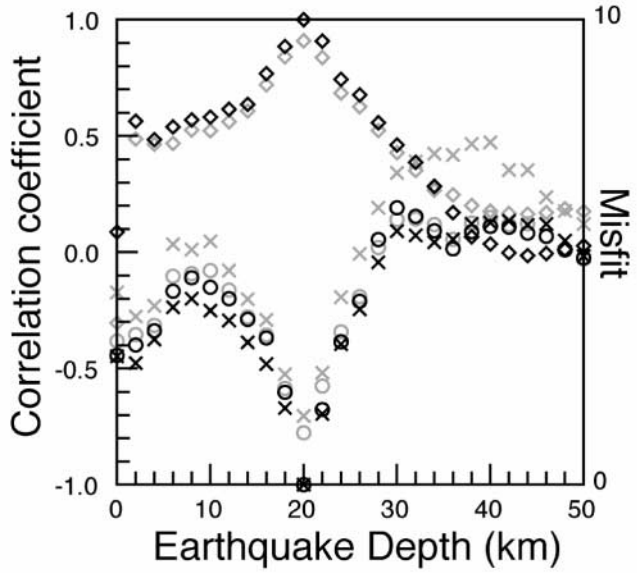

Figure 4. Correlation coefficient (diamonds) and L1 (circles) and L2 (x's) misfits between synthetic observations and predictions for earthquakes between 0 and 50 km depth. The synthetics (the same as in previous figures) are for an earthquake at 20 km depth, which is also the peak in the correlation coefficient and minima in the misfits. The black symbols represent calculations with the proper focal mechanism while the gray symbols represent computations with a 20° error in the strike of the focal mechanism.

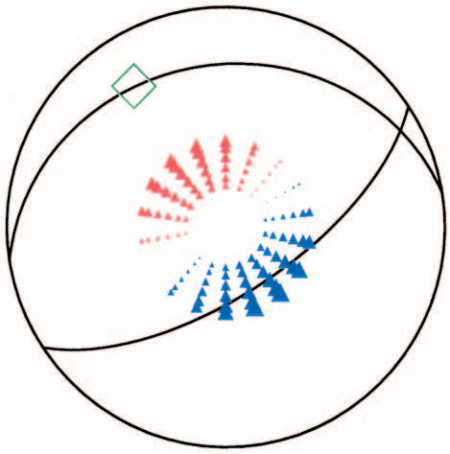

Figure 5. For an earthquake with the same focal mechanism as in the previous figures, we compute the spectral variations for a unilateral rupture that propagates entirely updip on the shallowly-dipping nodal plane (away from the direction marked by the green diamond). The blue triangles to the southeast indicate spectra enriched in high frequencies (i.e., correspond to seismograms with shorter pulse widths), while the red triangles to the northwest represent spectra depleted in high frequencies (i.e., correspond to seismograms with longer pulse widths). Note that no scale is indicated because the variations in pulse width depend on the size of the earthquake. For an M_w 5 event, the maximum difference in pulse widths over the entire focal sphere would be ~1 sec, while for an M_w 8 earthquake, the maximum difference could be > 30 sec.

Since these sets of terms are dependent on each other, the solution is obtained iteratively. First, we stack the appropriate spectra to find each source term T_i, assuming each station term R_j is zero, and then we use the T_i values to find R_j. These R_j terms are, in turn, used to find T_i and so on until stable solutions for T and R are found, generally after only a few iterations. The station stacks include the site response and near-receiver attenuation, while the earthquake stacks contain deviations from the average source model and near-source attenuation. We assume that attenuation around each earthquake and station is uniform. After correcting for the average source and attenuation models and source- and receiver-specific terms, the residual spectrum is

$$\log U'_{ij} = \log U_{ij} - \log \bar{S} - \log T_i - \log R_j - \log I_j - \log \bar{A} - \log G. \quad (6)$$

Since shallow variations in attenuation are absorbed in the source and receiver terms, the residual spectrum represents azimuthally-varying source effects T' (i.e., source complexity), interference P from depth phases, core reflections, and water reverberations that arrive during the signal window, and deep lateral variations in attenuation A'. We rewrite the residual spectrum in terms of these quantities:

$$\log U'_{ij} = \log T'_i(f,\theta) + \log P_i(f,\theta) + \log A'_{ij}(f) + b, \quad (7)$$

where θ is the angle from the rupture direction and b is a frequency-independent constant. Previous work has shown that lateral variations in attenuation in the lower mantle would have to be large in both magnitude and spatial extent to have a significant signal (Warren and Shearer, 2002), so we set $\log A'$ to 0. For shallow earthquakes, we interpret the remaining signal primarily as interference from other phases and use it to determine earthquake depths. However, when interpreting the results, we also consider the effect of rupture directivity.

Examples of Depth Determinations

Central Aleutian Islands Earthquakes

From the central Aleutian Islands near the Andreanof Islands, our earthquake catalog contains 35 shallow thrust events with similar focal mechanisms, as well as four shallow normal earthquakes, one shallow strike-slip event, and two deeper earthquakes (Figure 6). For the thrust events, we observe very consistent azimuthal variations in frequency content for earthquakes ranging from M_w 5.6 to M_w 7.9, as

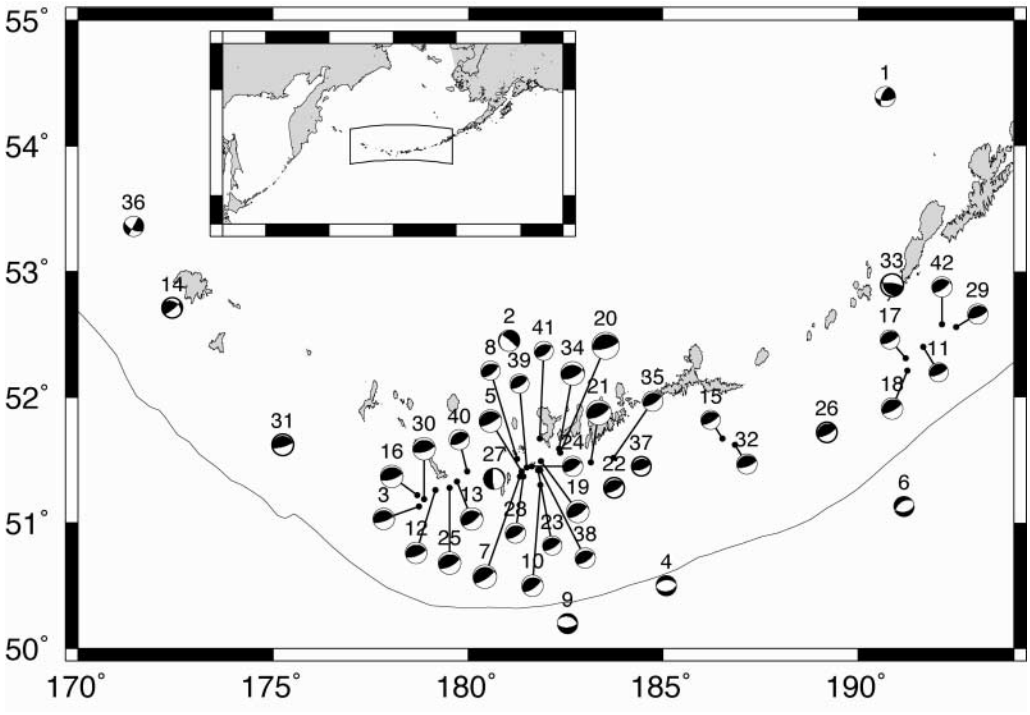

Figure 6. Locations and focal mechanisms for earthquakes in the Aleutian Islands near the Andreanof Islands. Refer to Table 1 to identify events by number.

shown in Figure 7 (a–c, middle column). If we interpret the spectral variations in terms of pulse width, there are longer than average durations to the northwest and shorter than average durations to the south and east along the more-steeply-dipping nodal plane. As listed in Table 1, 60% of these earthquakes are assigned an arbitrary depth of 33 km in the PDE catalog, while the remaining events are located at 43 km, 67 km, and between 11 and 32 km depth.

If we compare the observations with spectral variations predicted by interference from depth and other phases, we can locate 29 of the thrust earthquakes to between 13 and 21 km depth (Table 1). For each of these events, when we correlate the observations with predictions for an earthquake at the catalog depth ± 30 km, we usually find a peak in the correlation coefficient and minima in the L1 and L2 misfits at or near the same depth. For three of the thrust earthquakes, Figure 7(a–c) shows the correlation coefficient and misfits between observations and predictions for different earthquake depths and compares the observations with predictions for the depth with the smallest L1 misfit. (Ⓔ Plots for all the events in this region are available online at the SSA Web site.) The maximum correlation coefficients and minimum misfits for each event are summarized in Table 1. At the depth of the L1 minimum, the predictions are highly correlated with the observations, indicating that the depth phases dominate the signal and that azimuthal source variability is small. The maximum correlation coefficient is smaller for the largest event (10 June 1994, 4:03 UTC; number 20 in Table 1), suggesting that the pulse-width variations we observe, while still dominated by interference from depth phases, are also influenced by rupture directivity. McGuire *et al.* (2002) found a directivity ratio, the ratio of the velocity of the centroid position to the rupture velocity ($V_{centroid}/V_{rupture}$), of 0.72 ± 0.02 for this event, indicating a unilateral component to the rupture. Considering just the depth-phase-interference effects, we find a hypocentral depth of 19.1 ± 1.6 km for this event, while other analyses have reported hypocentral depths of 18 km (Tanioka and Ruff, 1997), 25 km (Schwartz, 1999), 28.0 km (Engdahl and Villaseñor, 2002), 33 km (USGS PDE), and 45 ± 10 km (Kisslinger and Kikuchi, 1997) and centroid depths of 9 km (USGS moment tensor solution) and 25 km (Harvard CMT).

For three thrust earthquakes, event numbers 11, 17, and 22, the bootstrap resampling depths cluster around multiple depths. In each case, one of the depths is between 13 and 21 km, as for the above events, but this depth does not have both the lowest L1 misfit and highest bootstrap-resampling percentage. A comparison of the observed variations in spectral content over the focal sphere for these three events, with the observed patterns for the 29 thrust events with well-determined depths, shows good agreement in regions where there are observations for both sets of earthquakes. This suggests that these three events may have occured in the same depth range. However, for these three events, the observations do not cover a broad enough portion of the focal sphere for us to conclusively identify their origin depths.

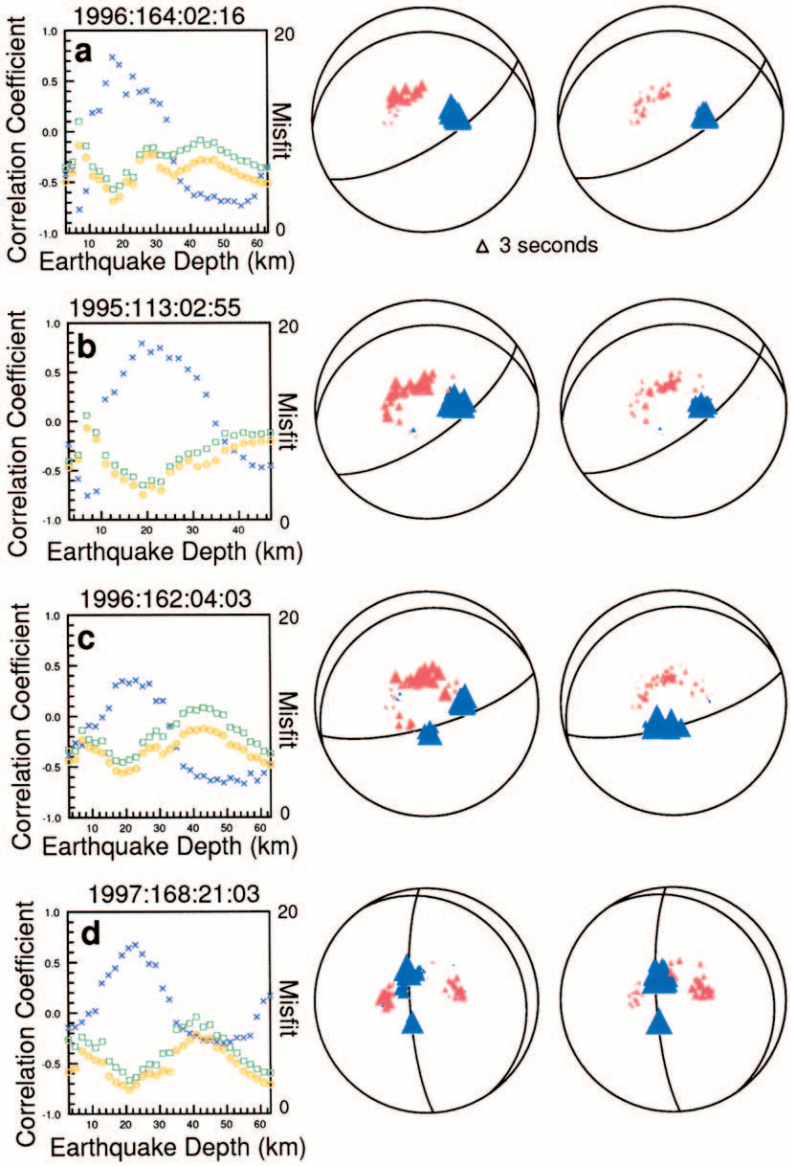

Figure 7. Observed and predicted variations in pulse width for select Aleutian Islands earthquakes. The first column contains plots of the correlation coefficient (purple x's), L1 misfit (orange circles), and L2 misfit (green squares) for different earthquake depths. The peak in the correlation and minima in the misfits indicate the best-fitting depth for the earthquake. The second column shows observed variations in frequency content, with blue indicating enrichment in high frequencies and red indicating depletion of high frequencies. The third column has predicted variations in frequency content for an earthquake at the depth corresponding to the L1 minimum. The plotted earthquakes are numbers 23 (a), 13 (b), 20 (c), and 27 (d) of Table 1. (Ⓔ Plots for all of the earthquakes listed in Table 1 are available online at the SSA Web site.)

The three additional thrust events that we cannot identify as originating between 13 and 21 km depth show coherent patterns of spectral variation different from the patterns observed for the other events. Since two of the events (numbers 33 and 41) originate significantly deeper (as determined by the PDE catalog and our analysis) than the main group, we would not expect to see the same focal sphere variations for them. The last event, number 42, does not have a clear misfit minimum. Instead, the misfits display a broad high between 20 km and 30 km depth, indicating that this event did not occur in this depth range.

A normal-faulting event in the Aleutians, number 27, is in the same area and depth range as the thrust events. As shown in Figure 7d, it also shows coherent variations in pulse width, but with a different pattern from the thrust events, that allow us to identify its focal depth as 21.0 ± 0.4 km.

The other three normal earthquakes in this region (numbers 4, 6, and 9) occur in the outer rise, rather than within the subducting slab, and have poorly-constrained L1-misfit minima at depths of 10.1 ± 4.0, 13.2 ± 2.4, and 4.7 ± 1.5 km, respectively, which are shallower than the thrust events. Events 4 and 9 have similar focal mechanisms and similar coherent patterns of observed variations in frequency content over the focal sphere, so we expect them to be located at similar depths, whereas event 6 shows smaller variations in frequency content over the focal sphere. For all three of these earthquakes, the correlation coefficients are relatively constant and near zero as the earthquake depth changes, and the misfits are fairly constant with earthquake depth down to about 20 km. The sharp increase in misfit at greater depths suggests that the earthquakes could not have originated in this depth range and likely occurred at shallower depths. However, we are unable to determine robust depths for these

Table 1
Dates and Locations of Aleutian Islands Earthquakes Plotted in Figure 6

No.	Date (year:day:hr:mn)	M_w	Latitude (° N)	Longitude (° E)	PDE Depth (km)	Engdahl Depth (km)	CC Depth, km (CC coefficient)	L1 Depth, km (m_{L1})	L2 Depth, km (m_{L2})
1	1991:226:12:53	6.0	54.3	190.7	274.0	277.3	—*	—	—
2	1992:073:16:01	6.4	52.5	180.1	197.0	199.9	—*	—	—
3	1992:155:06:10	6.2	51.2	178.8	21.0	24.6	18.1 ± 1.0 (0.47)	18.0 ± 1.3 (1.56)	17.9 ± 1.2 (1.86)
4	1992:232:00:57	6.1	50.5	185.1	9.0	16.7			
			42%/100%/100%				11.0 ± 0.0 (0.06)	10.1 ± 4.0 (4.54)	12.3 ± 3.7 (5.11)
			58%/—/—				39.0 ± 0.3 (0.14)	—	—
5	1992:274:05:34	6.6	51.3	181.9	33.0	20.7	19.8 ± 2.9 (0.88)	18.9 ± 0.7 (2.93)	19.4 ± 1.8 (3.95)
6	1993:104:05:58	5.9	51.3	190.2	33.0	19.9	21.6 ± 14.3 (−0.03)	13.2 ± 2.4 (2.05)	14.6 ± 2.8 (2.63)
7	1993:135:21:52	6.9	51.3	181.3	32.0	32.0	20.8 ± 1.0 (0.86)	22.8 ± 2.1 (4.81)	22.8 ± 1.7 (5.24)
8	1993:153:08:27	5.8	51.5	181.3	33.0	48.4	18.1 ± 2.3 (0.20)	17.5 ± 1.0 (2.13)	17.4 ± 0.9 (2.71)
9	1993:315:00:28	6.0	50.2	182.6	18.0	25.3			
			100%/97%/72%				4.0 ± 0.3 (0.81)	4.7 ± 1.5 (2.85)	4.1 ± 0.8 (4.04)
			—/—/28%				—	—	45.9 ± 0.4 (5.14)
10	1994:095:09:35	6.2	51.3	181.9	19.0	21.5	19.5 ± 2.2 (0.77)	19.0 ± 2.3 (3.88)	19.8 ± 2.7 (4.07)
11	1994:210:00:17	5.8	52.4	191.7	11.0	14.2			
			100%/70%/87%				8.6 ± 3.9 (0.27)	3.8 ± 1.1 (5.29)	4.7 ± 0.9 (7.51)
			—/24%/10%				—	15.1 ± 0.4 (3.88)	14.8 ± 0.6 (5.49)
12	1995:016:18:14	6.3	51.2	179.2	33.0	33.3			
			99%/83%/91%				18.6 ± 2.9 (0.47)	17.0 ± 0.4 (1.57)	17.0 ± 0.3 (1.85)
			—/17%/9%				—	60.5 ± 2.2 (2.02)	61.7 ± 1.7 (2.72)
13	1995:113:02:55	6.5	51.3	179.7	17.0	18.5	19.8 ± 1.6 (0.78)	19.2 ± 0.8 (2.15)	19.5 ± 1.3 (3.13)
14	1995:277:15:12	5.9	52.7	172.5	27.0	29.8	18.1 ± 1.7 (0.54)	18.3 ± 1.0 (2.11)	18.0 ± 1.0 (3.03)
15	1995:303:20:25	5.8	51.7	186.6	14.0	14.0			
			100%/87%/82%				21.0 ± 11.7 (−0.04)	17.3 ± 1.0 (1.48)	17.6 ± 0.9 (1.81)
			—/13%/18%				—	36.5 ± 0.9 (1.96)	36.6 ± 0.9 (2.25)
16	1996:082:03:24	6.7	51.2	178.7	20.0	21.5	19.8 ± 0.5 (0.70)	20.0 ± 0.3 (2.14)	19.9 ± 0.5 (2.51)
17	1996:088:19:51	5.8	52.3	191.2	33.0	17.3			
			19%/26%/19%				3.0 ± 0.0 (0.11)	3.0 ± 0.0 (2.06)	3.0 ± 0.0 (2.43)
			44%/32%/29%				18.2 ± 3.9 (0.17)	15.3 ± 1.0 (2.04)	15.6 ± 0.9 (2.43)
			22%/6%/6%				34.8 ± 3.9 (−0.17)	37.7 ± 1.0 (2.46)	37.0 ± 0.0 (2.59)
			15%/36%/46%				60.5 ± 3.5 (0.03)	59.1 ± 3.4 (2.15)	60.5 ± 2.9 (2.38)
18	1996:090:13:05	6.3	52.2	191.3	33.0	19.4	19.0 ± 0.4 (0.62)	19.0 ± 0.0 (2.86)	19.0 ± 0.0 (4.06)
19	1996:160:23:19	6.5	51.5	181.9	33.0	29.0	20.3 ± 3.0 (0.90)	19.2 ± 1.6 (3.00)	18.4 ± 2.3 (5.20)
20	1996:162:04:03	7.9	51.6	182.4	33.0	28.0	20.3 ± 3.0 (0.39)	19.1 ± 1.6 (4.22)	18.8 ± 1.2 (5.43)
21	1996:162:15:24	7.3	51.5	183.1	26.0	27.5	18.1 ± 0.5 (0.84)	20.0 ± 0.0 (2.96)	20.0 ± 0.0 (3.71)
22	1996:163:10:40	5.9	51.3	183.7	33.0	20.7			
			100%/80%/76%				6.4 ± 1.4 (0.37)	5.0 ± 0.0 (1.59)	4.7 ± 0.9 (11.62)
			—/7%/7%				—	15.0 ± 0.0 (1.86)	15.0 ± 0.0 (2.71)
			—/13%/17%				—	62.8 ± 0.6 (1.94)	62.8 ± 1.0 (2.56)
23	1996:164:02:16	5.8	51.4	181.8	33.0	26.0	17.7 ± 1.5 (0.73)	17.3 ± 0.7 (3.23)	17.4 ± 1.2 (4.50)
24	1996:232:04:19	6.0	51.5	181.6	33.0	28.0	18.5 ± 1.6 (0.68)	18.0 ± 1.0 (3.34)	18.3 ± 1.7 (4.42)
25	1997:085:02:08	6.7	51.3	179.5	33.0	28.0	18.0 ± 1.0 (0.60)	18.1 ± 1.0 (2.61)	18.1 ± 1.0 (3.01)
26	1997:128:13:29	6.0	51.7	189.2	33.0	20.2	18.8 ± 2.2 (0.39)	17.1 ± 2.0 (2.46)	17.3 ± 1.9 (2.97)
27	1997:168:21:03	6.4	51.4	180.7	33.0	25.6			
			100%/95%/98%				22.5 ± 1.0 (0.68)	21.0 ± 0.4 (2.35)	21.2 ± 0.6 (3.38)
			—/5%/—				—	63.0 ± 0.0 (2.84)	—
28	1997:189:12:11	5.9	51.4	181.4	33.0	26.0	17.6 ± 1.7 (0.74)	17.8 ± 1.0 (3.71)	17.7 ± 1.4 (4.43)
29	1997:201:00:30	6.1	52.6	192.5	14.0	17.9	18.3 ± 0.9 (0.59)	20.0 ± 0.0 (0.90)	19.8 ± 0.6 (2.11)
30	1997:351:04:38	6.6	51.2	178.9	20.0	20.7	22.8 ± 2.5 (0.21)	18.0 ± 0.6 (2.35)	18.0 ± 0.3 (2.68)
31	1998:232:15:00	6.2	51.6	175.2	33.0	13.2	18.4 ± 0.9 (0.47)	18.9 ± 0.4 (2.36)	18.2 ± 1.0 (3.46)
32	1998:257:23:16	6.1	51.6	186.8	33.0	17.3	17.3 ± 0.9 (0.63)	17.0 ± 0.0 (1.81)	17.0 ± 0.3 (2.34)
33	1999:028:08:10	6.6	52.9	190.9	67.0	59.0	37.4 ± 1.9 (0.35)	62.1 ± 2.2 (3.36)	62.6 ± 2.3 (4.56)
34	1999:079:10:47	6.9	51.6	182.3	33.0	33.0			
			43%/93%/98%				17.0 ± 0.0 (0.26)	15.2 ± 0.6 (2.24)	16.2 ± 1.0 (2.97)
			57%/—/—				35.7 ± 2.7 (0.21)	—	—
			—/7%/—				—	61.0 ± 0.0 (2.58)	—
35	1999:213:12:47	5.9	51.5	183.7	33.0	34.0	17.3 ± 0.8 (0.77)	18.3 ± 1.8 (4.04)	17.2 ± 0.8 (3.90)
36	1999:317:19:31	5.9	53.4	171.4	33.0	23.3			
			—/—/9%				—	—	3.0 ± 0.0 (3.68)
			90%/36%/38%				16.6 ± 8.9 (0.12)	18.4 ± 1.9 (1.81)	18.4 ± 1.1 (2.37)

(*continued*)

Table 1
Continued

No.	Date (year:day:hr:mn)	M_w	Latitude (° N)	Longitude (° E)	PDE Depth (km)	Engdahl Depth (km)	CC Depth, km (CC coefficient)	L1 Depth, km (m_{L1})	L2 Depth, km (m_{L2})
			—/12%/10%				—	31.2 ± 0.6 (2.36)	31.2 ± 0.6 (3.32)
			10%/48%/43%				63.0 ± 0.0 (0.12)	62.9 ± 0.5 (1.61)	62.8 ± 1.0 (2.29)
37	2000:002:12:58	5.8	51.5	184.4	33.0	40.5	19.2 ± 3.9 (0.01)	14.9 ± 1.8 (3.39)	15.7 ± 1.9 (4.61)
38	2000:112:04:35	6.0	51.4	181.9	33.0	28.0	21.1 ± 2.1 (0.50)	18.1 ± 1.5 (2.78)	21.1 ± 2.2 (3.98)
39	2000:125:14:24	5.6	51.4	181.5	33.0	29.0			
			0%/20%/14%				—	4.9 ± 0.4 (2.82)	3.3 ± 0.7 (4.28)
			89%/75%/82%				15.0 ± 5.9 (0.03)	15.0 ± 0.8 (2.70)	15.3 ± 0.8 (4.15)
			9%/—/—				43.9 ± 1.8 (−0.44)	—	—
40	2000:189:15:46	5.9	51.4	180.0	31.0	31.0			
			11%/97%/98%				14.3 ± 1.8 (0.03)	15.4 ± 0.8 (2.12)	15.8 ± 1.0 (2.81)
			89%/—/—				41.5 ± 5.0 (0.25)	—	—
41	2000:338:12:55	5.7	51.7	181.8	43.0	50.8			
			13%/43%/17%				13.0 ± 0.0 (0.02)	13.0 ± 0.0 (5.28)	13.0 ± 0.0 (7.51)
			81%/55%/78%				48.3 ± 1.6 (0.67)	46.3 ± 2.8 (5.04)	48.4 ± 1.7 (5.56)
			6%/—/5%				73.0 ± 0.0 (0.14)	—	72.2 ± 1.8 (7.39)
42	2000:340:22:11	5.9	52.6	192.1	33.0	30.1			
			95%/85%/95%				4.3 ± 0.9 (−0.46)	4.9 ± 0.4 (4.13)	4.9 ± 0.4 (6.04)
			—/15%/5%				—	52.3 ± 3.3 (4.48)	51.8 ± 1.8 (6.97)

Comparison of catalog depths with depths of maximum correlation coefficents and minimum misfits found in this analysis. When the error analysis provides depths in two (or more) distinct clusters, the depths are reported on separate lines and the frequency of each depth is noted on the left. Only depths found ≥5% of the time are reported.

*Events 1 and 2 are much deeper than the other events in the region, so the depth phases and core reflections have little effect on the spectrum and resulting azimuthal variations in pulse width, and we do not report improved depths for them.

earthquakes, and it is unclear whether this is a result of insufficient focal sphere coverage or uncertainty introduced by the water column reverberations for earthquakes less than ~10 km depth.

1995 Jalisco Mexico Earthquake: A Unilateral Event

If we apply the same analysis to earthquakes with strongly unilateral ruptures, we generally cannot explain our observations with interference from depth phases. For example, McGuire *et al.* (2002) found that the directivity ratio for the 9 October 1995 Jalisco, Mexico, event was 0.88 ± 0.07. For this event, the mismatch between the spectral variations that we observe (Fig. 8b) and the spectral variations that we predict from depth-phase interference can be seen in the consistently near-zero correlation coefficient and near-constant misfit with changing earthquake depth (Fig. 8a). We find a minimum in the L1 misfit at 19 km depth, although this fit is only slightly better than for an origin depth of 14.4 ± 0.7 km (as reported by McGuire *et al.*, 2001) or 17 km (as reported by Courboulex *et al.*, 1997). Aside from small values on the nodal planes, the predicted spatial variations in spectral content for a point source at 19 km depth (Fig. 8c) show little variability over the focal sphere and do not match the observations, which have large amplitude variations over the entire focal sphere, with the shortest durations to the northwest.

Since the amplitude of the signal predicted by the depth phases is less than half the amplitude of the observed signal, we interpret the spectral variations for this event solely in terms of *P*-wave directivity. For each direction on the focal sphere, we compare the observed variations in spectral content to a model of purely unilateral rupture in that direction. Next, we estimate the misfit, relative to a point source, for each direction and find that rupture updip towards an azimuth of 270° (Fig. 8d) provides the best fit to the observations. Previous work (McGuire *et al.*, 2001) has shown that the rupture propagated towards an azimuth of 307° on the shallowly-dipping nodal plane. The spectral variations predicted for unilateral rupture in this direction, which are plotted in Figure 8e, largely replicate the observed spatial patterns of enrichment in and depletion of high-frequency energy. Thus, for this example, the spectral variations appear to be dominated by the rupture directivity but, in general, this method does not allow us to entirely separate the effects of directivity and the depth phases.

Discussion

While an earthquake's depth generally trades off with the origin time of the event, it can be constrained by the relative timing and amplitudes of the primary arrival and the ensuing depth phases, core reflections, and water reverberations. For earthquakes shallower than ~150–200 km depth, we have developed a systematic method to estimate how the later arrivals change the *P*-wave spectrum, specifically whether they enrich or deplete it in high frequencies, and then to correlate these observations over the focal sphere with predicted spectral variations to determine earthquake depth.

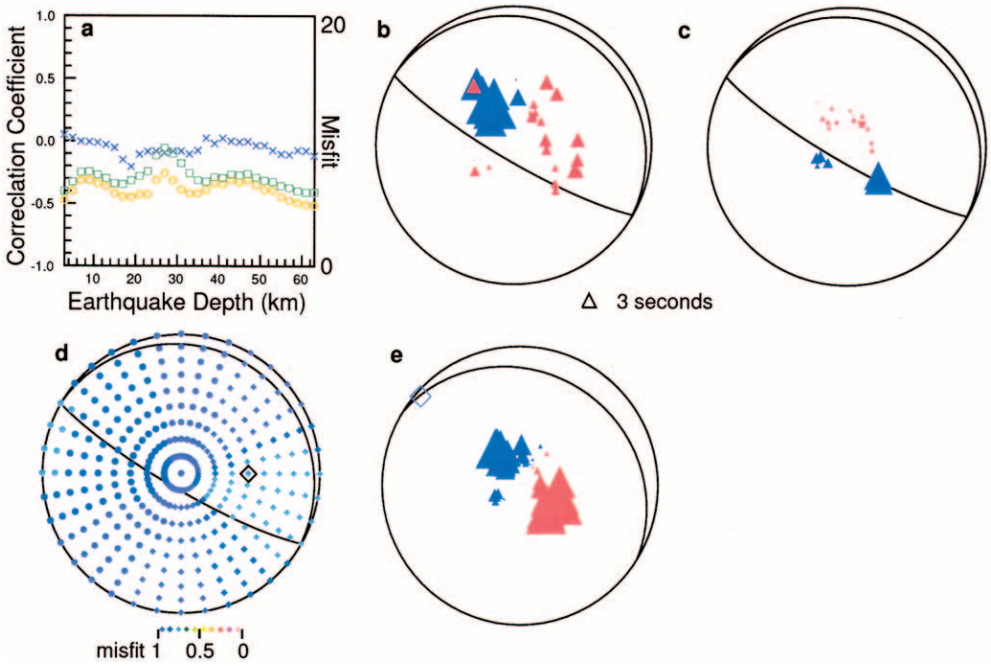

Figure 8. Analysis of the 9 October 1995 Jalisco, Mexico, M_w 8.0 earthquake. Observed variations in frequency content (b) cannot be interpreted as interference from depth phases and core reflections (a, c) but more closely resemble rupture directivity (d, e). (a–c) Description as in Figure 7, with (c) showing predicted variations in pulse width for an earthquake at 19 km depth. (d) The observed variations in pulse width are compared with a model of purely unilateral rupture in each direction on the focal sphere and the misfit, relative to a point source, is plotted. The best-fitting rupture direction is updip and away from the direction indicated by the black diamond. (e) Predicted variations in pulse width for unilateral rupture in direction (indicated by purple diamond) found by McGuire *et al.* (2001).

The main advantages of this method are that it is automated, fast, and not sensitive to location errors or travel time anomalies. Since we compute the spectrum for a long time window, shifting the timing of the window by several seconds—which could be caused by location errors or the velocity structure the waves propagate through—does not alter the resulting spectrum significantly. Using spectral variations to estimate earthquake depth is faster than visually inspecting each seismogram to pick the arrival times of each phase, and can be used at longer periods when the depths phases are not always separable from the primary arrival. As a result, this method is well-suited for research topics ranging from analyzing and tabulating depths for a large catalog of existing earthquakes to estimating the depth of an earthquake shortly after it occurs for seismic hazard assessment or discriminating it from a nuclear explosion.

One shortcoming is that, at present, this method does not account for azimuthal variations in the source-time history of the rupture process. As a result, when we apply this method to strongly directive earthquakes, we generally cannot recover the earthquake depth. As we demonstrated for the 1995 Jalisco, Mexico, event, the observed spectral variations more closely resemble the predicted spectral variations for a unilateral rupture than for interference from depth phases. To better explain the observations, the next step is to jointly model the effects of directivity and the later-arriving phases on the spectra, and how the resulting spectra vary over the focal sphere.

Many earthquakes in the global catalog, particularly the smaller events, are well-represented by a point source, and this method already allows us to determine better depths for them. For example, a group of thrust events in the central Aleutian Islands near the Andreanof Islands show very consistent focal-sphere patterns of enrichment and depletion in high-frequency energy that allow us to locate 29 of the 35 events to between 13 and 21 km depth. This provides a much tighter constraint than the PDE catalog depths, which range between 11 and 32 km, in addition to many arbitrarily-assigned depths of 33 km. Since we have a catalog of thousands of additional shallow earthquakes, there are other regions where the distribution of earthquake depths can help us understand the regional tectonics and fault structures.

Since this method works best when observations are distributed at a range of azimuths and distances, the only geographic limitations on where this method can be applied come from the distribution of seismometers relative to earthquakes and the occurence of earthquakes large enough to be recorded around the Earth. While we have studied earth-

quakes with $M_w \geq 5.5$ and found depths for earthquakes up to M_w 7.9, the analysis for the larger events is less certain because they have more complex rupture histories. Thus, this method is best-suited for earthquakes between about M_w 5.5 and M_w 6.5. The region we studied was dominated by thrust events, but there is nothing special about thrust events that makes them more suitable for this type of analysis than normal or strike-slip events. For this method to be applicable, it is only necessary that the depth phases arrive within the time window for which the spectrum is computed, which corresponds to earthquakes down to about 150 km depth.

Acknowledgments

We thank Heidi Houston and John Vidale for discussions, Guy Masters for use of his long-period seismic database, and Frank Vernon for providing his multitaper routines. Heidi Houston and Keith Koper provided constructive reviews that improved this paper. This work was supported by National Science Foundation grants EAR-99-09267 and EAR-02-29323.

References

Bollinger, G. A. (1968). Determination of earthquake fault parameters from long-period *P* waves, *J. Geophys. Res.* **73,** 785–807.

Bolton, H., and G. Masters (2001). Travel times of *P* and *S* from the global digital seismic networks: Implications for the relative variation of *P* and *S* velocity in the mantle, *J. Geophys. Res.* **106,** 13,527–13,540.

Bonner, J. L., D. T. Reiter, and R. H. Shumway (2002). Application of a cepstral *F* statistic for improved depth estimation, *Bull. Seism. Soc. Am.* **92,** 1675–1693.

Centroid Moment Tensor (CMT) Catalog, www.seismology.harvard.edu/CMTsearch.htm/.

Childers, D. B., D. P. Skinner, and R. C. Kemerait (1977). The cepstrum: A guide to processing, *Proc. IEEE* **65,** 1428–1443.

Cohen, T. J. (1970). Source-depth determinations using spectral, pseudo-autocorrelation and cepstral analysis, *Geophys. J. R. Astr. Soc.* **20,** 223–231.

Courboulex, F., S. K. Singh, J. F. Pacheco, and C. J. Ammon (1997). The 1995 Colima-Jalisco, Mexico, earthquake (M_w 8): A study of the rupture process, *Geophys. Res. Lett.* **24,** 1019–1022.

Dziewonski, A. M., and D. L. Anderson (1981). Preliminary reference Earth model (PREM), *Phys. Earth Planet. Interiors* **25,** 297–365.

Efron, B. (1982). The Jackknife, the Bootstrap and Other Resampling Plans in *CBMS-NSF Reg. Conf. Ser. Appl. Math.*, Soc. for Ind. and Appl. Math., **38,** Philadephia, PA.

Engdahl, E. R., and A. Villaseñor (2002). Global Seismicity: 1990–1999, in *International Handbook of Earthquake and Engineering Seismology, Part A*, W. H. K. Lee, H. Kanamori, P. C. Jennings, and C. Kisslinger (Editors), Academic Press, New York, 665–690.

Engdahl, E. R., R. van der Hilst, and R. Buland (1998). Global teleseismic earthquake relocation with improved travel times and procedures for depth determination, *Bull. Seism. Soc. Am.* **88,** 722–743.

Haskell, N. A. (1964). Total energy and energy spectral density of elastic wave radiation from propagating faults, *Bull. Seism. Soc. Am.* **54,** 1811–1841.

Houston, H., and H. Kanamori (1986). Source spectra of great earthquakes: Teleseismic constraints on rupture process and strong motion, *Bull. Seism. Soc. Am.* **76,** 19–42.

Kennett, B. L. N. (1991). *IASPEI 1991 Seismological Tables*, Res. Sch. of Earth Sci., Aust. Nat. Univ., Canberra.

Kisslinger, C., and M. Kikuchi (1997). Aftershocks of the Andreanof Islands earthquake of June 10, 1996, and local seismotectonics, *Geophys. Res. Lett.* **24,** 1883–1886.

McGuire, J. J., L. Zhao, and T. H. Jordan (2001). Teleseismic inversion for the second-degree moments of earthquake space-time distributions, *Geophys. J. Int.* **145,** 661–678.

McGuire, J. J., L. Zhao, and T. H. Jordan (2002). Predominance of unilateral rupture for a global catalog of large earthquakes, *Bull. Seism. Soc. Am.* **92,** 3309–3317.

Park, J., C. R. Lindberg, and F. L. Vernon, III (1987). Multitaper spectral analysis of high-frequency seismograms, *J. Geophys. Res.* **92,** 12,675–12,684.

Schwartz, S. Y. (1999). Noncharacteristic behavior and complex recurrence of large subduction zone earthquakes, *J. Geophys. Res.* **104,** 23,111–23,125.

Sipkin, S. A. (2000). The use of waveform shapes to automatically determine earthquake focal depth, *Bull. Seism. Soc. Am.* **90,** 248–254.

Tanioka, Y., and L. J. Ruff (1997). Source time functions, *Seism. Res. Lett.* **68,** 386–400.

Thomson, D. J. (1982). Spectrum estimation and harmonic analysis, *Proc. IEEE* **70,** 1055–1096.

Warren, L. M. (2003). Analysis of global compressional-wave spectra to determine anelastic Earth structure and earthquake rupture directivity, *Ph.D. Thesis*, University of California, San Diego.

Warren, L. M., and P. M. Shearer (2000). Investigating the frequency dependence of mantle *Q* by stacking *P* and *PP* spectra, *J. Geophys. Res.* **105,** 25,391–25,402.

Warren, L. M., and P. M. Shearer (2002). Mapping lateral variations in upper mantle attenuation structure by stacking *P* and *PP* spectra, *J. Geophys. Res.* **107,** doi:10.1029/2001JB001195.

IGPP, SIO, UCSD
9500 Gilman Drive
La Jolla, California 92093-0225
pshearer@ucsd.edu
(P.M.S.)

Dept. of Terrestrial Magnetism
Carnegie Institution of Washington
5241 Broad Branch Rd., N.W.
Washington, D.C. 20015
warren@dtm.ciw.edu
(L.M.W.)

Manuscript received 12 January 2004.